Structural differences between yeast and mammalian microtubules revealed by cryo-EM

Stuart C. Howes,[1] Elisabeth A. Geyer,[5,6] Benjamin LaFrance,[2] Rui Zhang,[3,7] Elizabeth H. Kellogg,[3,7] Stefan Westermann,[8] Luke M. Rice,[5,6] and Eva Nogales[3,4,7]

[1]Biophysics Graduate Group, [2]Molecular and Cell Biology Graduate Program, [3]Howard Hughes Medical Institute, and [4]Department of Molecular Biology and California Institute for Quantitative Biosciences, University of California, Berkeley, Berkeley, CA
[5]Department of Biophysics and [6]Department of Biochemistry, University of Texas Southwestern Medical Center, Dallas, TX
[7]Molecular Biophysics and Integrated Bioimaging Division, Lawrence Berkeley National Laboratory, Berkeley, CA
[8]Department of Molecular Genetics, Center for Medical Biotechnology, University of Duisburg-Essen, Essen, Germany

Microtubules are polymers of αβ-tubulin heterodimers essential for all eukaryotes. Despite sequence conservation, there are significant structural differences between microtubules assembled in vitro from mammalian or budding yeast tubulin. Yeast MTs were not observed to undergo compaction at the interdimer interface as seen for mammalian microtubules upon GTP hydrolysis. Lack of compaction might reflect slower GTP hydrolysis or a different degree of allosteric coupling in the lattice. The microtubule plus end–tracking protein Bim1 binds yeast microtubules both between αβ-tubulin heterodimers, as seen for other organisms, and within tubulin dimers, but binds mammalian tubulin only at interdimer contacts. At the concentrations used in cryo-electron microscopy, Bim1 causes the compaction of yeast microtubules and induces their rapid disassembly. Our studies demonstrate structural differences between yeast and mammalian microtubules that likely underlie their differing polymerization dynamics. These differences may reflect adaptations to the demands of different cell size or range of physiological growth temperatures.

Introduction

Microtubules (MTs) are formed by the polymerization of αβ-tubulin heterodimers into hollow, cylindrical polymers that constitute an essential component of the eukaryotic cytoskeleton. MTs play a pivotal role in organizing the cellular contents (Desai and Mitchison, 1997; Conde and Cáceres, 2009) and forming the mitotic spindle that is crucial for cell division (Ward et al., 2014; Heald and Khodjakov, 2015). Central to MT functionality is the ability of the cell to reorganize the MT network, both during the cell cycle and in response to environmental cues. This remodeling is achieved by the coordinated actions of MT-associated proteins (MAPs) that organize, stabilize, or destabilize MTs. Proteins that specifically bind the growing ends of MTs (+TIPs) are a particularly important class of MAPs that significantly influence MT behaviors (Akhmanova and Steinmetz, 2008; Kumar and Wittmann, 2012). This regulation builds on the property of dynamic instability, by which MTs undergo GTPase-dependent stochastic transitions between growing and shrinking phases (Mitchison and Kirschner, 1984; Desai and Mitchison, 1997). Both α- and β-tubulin bind one GTP molecule. The GTP bound to α-tubulin, at the nonexchangeable site (N-site), plays a structural role and is never hydrolyzed, whereas the GTP bound to β-tubulin, at the exchangeable site (E-site), is hydrolyzed within the MT upon polymerization, a process catalyzed by residues in α-tubulin interacting across an interdimer interface (Nogales et al., 1998). Recent high-resolution cryo-EM studies using mammalian tubulin have shown that GTP hydrolysis results in compaction at the interdimer interface that involves conformational changes in α-tubulin (Alushin et al., 2014; Zhang et al., 2015). Those structural studies are consistent with a model in which the MT switches from a growing phase to a shrinking phase because of conformational strain stored within the lattice that is released during MT depolymerization.

The central importance of MTs has led to extensive research to understand the mechanistic origins of dynamic instability. For the overwhelming majority of in vitro experiments, the source of tubulin has been mammalian brain tissue, where tubulin constitutes almost 25% of the total protein content (Hiller and Weber, 1978). This convenient source is, however, not amenable to the study of tubulin mutants. Efforts to produce recombinant tubulin (Minoura et al., 2013; Ti et al., 2016; Valenstein and Roll-Mecak, 2016) and to purify tubulin from differ-

Correspondence to Eva Nogales: enogales@lbl.gov

S.C. Howes's present address is Dept. of Molecular Cell Biology, Leiden University Medical Center, Leiden, Netherlands.

R. Zhang's present address is Dept. of Biochemistry and Molecular Biophysics, Washington University School of Medicine, St. Louis, MO.

Abbreviations used: CH, calponin homology; E-site, exchangeable site; EB, end binding; MT, microtubule; N-site, nonexchangeable site; PF, protofilament.

The Rockefeller University Press
J. Cell Biol. Vol. 216 No. 9 2669–2677
https://doi.org/10.1083/jcb.201612195

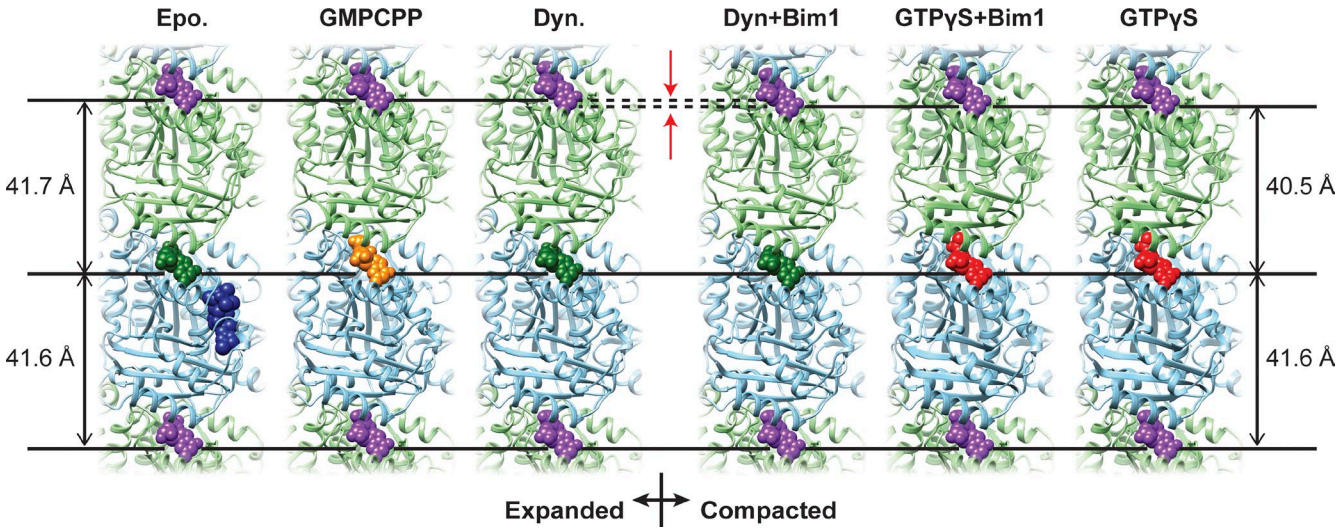

Figure 1. **Lattice distinctions for yeast MTs.** Models of two tubulin dimers from a PF for the indicated state. Expanded lattices (epothilone, GMPCPP, and dynamic) and compacted lattices (Dyn+Bim1, GTPγS+Bim1, and GTPγS) are distinguished by compaction across the interdimer interface, reducing the interdimer nucleotide distance (indicated by red arrows). Distances between nucleotides are given for epothilone and GTPγS (see Table S1 for exact values). Epothilone (dark blue), GTP (purple), GDP (dark green), GMPCPP (orange), and GTPγS (red) are shown with space-filled spheres; α-tubulin is shown in green and β-tubulin in blue. Note that in the dynamic lattice, a mixture of GTP and GDP is likely present at the E-site (see main text).

ent sources (Davis et al., 1993; Yoon and Oakley, 1995; Sackett et al., 2010; Drummond et al., 2011; Widlund et al., 2012) have recently been successful but have not yet been widely adopted. On the other hand, genetically approachable organisms, such as budding yeast, have for a long time been used to characterize temperature- and drug-sensitive mutants and thus probe the functionality of different parts of tubulin in vivo (Thomas et al., 1985; Schatz et al., 1988; Reijo et al., 1994; Fackenthal et al., 1995; Machin et al., 1995; Richards et al., 2000). A large body of knowledge about yeast tubulin mutants has provided important insights into MT functionality, but the mechanistic origin of different tubulin mutation phenotypes is generally unknown.

Carefully designed overexpression systems have made possible the purification of tubulin from *Saccharomyces cerevisiae* (hereafter referred to as yeast), even for tubulin mutants that are lethal under normal circumstances (Johnson et al., 2011; Ayaz et al., 2012; Geyer et al., 2015). This method now yields sufficient quantities of yeast tubulin for biophysical and structural characterization and opens the door for comparative studies between mammalian and yeast tubulins/MTs. Here we have used high-resolution cryo-EM to visualize yeast MTs in different nucleotide- and drug-bound states. In contrast to our prior studies of mammalian MTs (Alushin et al., 2014; Zhang et al., 2015), we observed a compacted state of the yeast MT lattice only in the presence of the +TIP protein Bim1 (an end-binding [EB] homolog). We also find that Bim1 binds both between αβ-tubulin dimers, as seen for other organisms, and within dimers. These findings have repercussions for our understanding of dynamic instability and its conservation across eukaryotes.

Results and discussion

The yeast MT lattice is expanded compared with mammalian MTs

Our previous cryo-EM work with mammalian tubulin described the changes that accompany GTP hydrolysis in the MT lattice (Alushin et al., 2014; Zhang et al., 2015), namely, a conformational change in α-tubulin around the region that contacts the E-site nucleotide at the longitudinal contact between dimers. This conformational response of α-tubulin to GTP hydrolysis results in a clear change in the MT lattice (measured by a reduction in the dimer rise, i.e., axial repeat) from an extended lattice when bound to GMPCPP to a compacted lattice when GTP is hydrolyzed to GDP. We found a similar extended lattice in terms of axial repeat for yeast MTs assembled from GMPCPP-bound tubulin or GTP-tubulin and stabilized with epothilone, a taxane-site binder with stabilizing effects similar to those of Taxol (Fig. 1). But, in contrast to what is seen for mammalian MTs, we observed that dynamic yeast MTs (assembled with GTP) displayed an expanded conformation, with a dimer rise of 83.3 Å, a size that would presumably correspond to the prehydrolysis state of the MT (Hyman et al., 1995; Alushin et al., 2014; Zhang et al., 2015). Possible explanations for this failure to compact include a reduced amount of GTP hydrolysis in yeast MTs or a dampening in the conformational response to the hydrolysis process, at least concerning the most tangible effect of lattice compaction. In contrast to the almost identical, expanded lattice for dynamic and GMPCPP-stabilized yeast MTs, we observed that the GTPγS lattice of yeast MTs was compacted by 1.2 Å. Our prior study of EB3-bound GTPγS mammalian MTs, which we proposed to provide a model for the GDP-Pi state of the lattice, showed 1.5-Å lattice compaction (Zhang et al., 2015). Lesser compaction of yeast MTs with GTPγS might reflect a greater propensity for expanded conformations. Because EB proteins are thought to bind preferentially to more compacted forms of tubulin (Maurer et al., 2012, 2014; Zhang et al., 2015), we also examined whether Bim1 binding to yeast MTs affected tubulin conformation in the lattice. We found that when Bim1 was bound to GTPγS yeast MTs, the lattice became fully compacted. This is not an artifact of GTPγS, because coassembly of dynamic yeast MTs with Bim1 also resulted in a compact lattice (see section Bim1 binds yeast MTs both within and between tubulin dimers). Full lattice parameters are given in Table S1.

To better characterize the conformations we observed for yeast MTs, we compared the high-resolution cryo-EM struc-

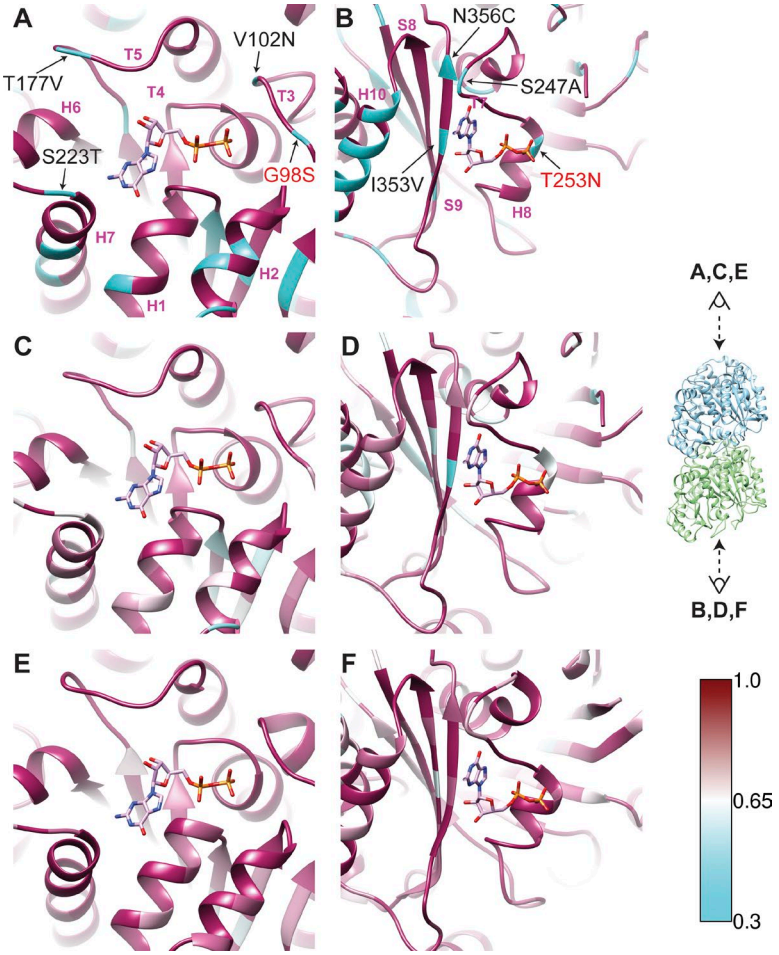

Figure 2. **Tubulin conservation around the E-site.** (A and B) View from plus end (A) and minus end (B) of the MT showing sequence conservation around the E-site nucleotide between yeast and mammalian tubulin. Identical and nonidentical residues are colored maroon and cyan, respectively. Nonconservative substitutions are labeled, with mammalian residue first, whereas conservative changes are not labeled. The changes (labeled in red text) at positions 98 on β-tubulin and 253 on α-tubulin potentially create a tighter pocket for the nucleotide in yeast tubulin. (C–F) Conservation of residues surrounding the E-site across fungal tubulins (C and D) and mammalian tubulins (E and F). Fungal tubulins are generally less conserved than mammalian tubulins, though similar positions (end of H10 and position 353 in S9, both on α-tubulin) are less conserved for both.

tural models of αβ-tubulin in GMPCPP-stabilized, dynamic, and drug-bound yeast MTs (Fig. S1) to the various states of mammalian tubulin we described previously (note that our previous analyses demonstrated that the structure of the tubulin heterodimer does not vary greatly between MTs that differ only by protofilament [PF] number; Alushin et al., 2014; Zhang et al., 2015). This comparison revealed that the conformation of αβ-tubulin in dynamic MTs, GMPCPP-MTs, or drug-stabilized yeast MTs was essentially the same as the expanded conformation we observed in mammalian GMPCPP-stabilized MTs (Fig. 1). To distinguish whether the expanded conformation of dynamic yeast MTs results from reduced GTPase activity or an altered conformational response to GDP would require knowledge about the nucleotide state. Unfortunately, analysis of the density in our cryo-EM reconstructions at the E-site is inconclusive with respect to the presence of GTP, GDP, or a mixture. This is likely because our current image-processing methods are unable to deal with the apparent existence of multiple seams in a fraction of our yeast MTs (Fig. S3), which in turn results in some mixing of the α- and β-tubulin structures, and consequently of the densities for the E-site and N-site nucleotides (see Materials and methods for details).

To identify possible sequence determinants of the slower GTPase or a different conformational response to GDP, we examined the structures in the vicinity of the exchangeable nucleotide binding site. Tubulin displays particularly high sequence conservation around the E-site nucleotide (Fig. 2), but there are nevertheless two interesting amino acid substitutions between the mammalian and yeast sequences (Fig. 2, A and B) that may contribute to the observed differences: G98 on the phosphate-contacting T3 loop of β-tubulin is replaced by S in yeast, and across the longitudinal interface that completes the E-site nucleotide binding pocket, T253 on H8 of α-tubulin is replaced by N in yeast tubulin. In both cases, the yeast substitution is to a larger side chain, creating a tighter pocket around the phosphate. We speculate that this geometry of the E-site in yeast tubulin results in less-efficient GTP hydrolysis or an attenuated conformational response to Pi release.

Bim1 binds yeast MTs both within and between tubulin dimers

Plus-tip tracking of growing MTs relies on a preference of EB proteins for a unique structural feature at the MT plus end (i.e., the dynamic end, which is capped by β-tubulin). Such a structural feature has been proposed to correspond to a distinct region near the GTP cap that is best mimicked by GTPγS MTs (Maurer et al., 2011, 2012; Zhang et al., 2015). Cryo-EM structures of human EB3 and fission yeast Mal3 bound to mammalian MTs have shown that these EB proteins bind between tubulin dimers and across PFs (Maurer et al., 2012; Zhang et al., 2015), in a position that would be most sensitive to changes in lattice parameters accompanying GTP hydrolysis. A recent study reported that Bim1 was an inefficient plus end tracker in assays using vertebrate MTs (Molodtsov et al., 2016), in contrast to prior work from one of our laboratories showing apparently normal plus end tracking of Bim1 on yeast MTs (Geyer et

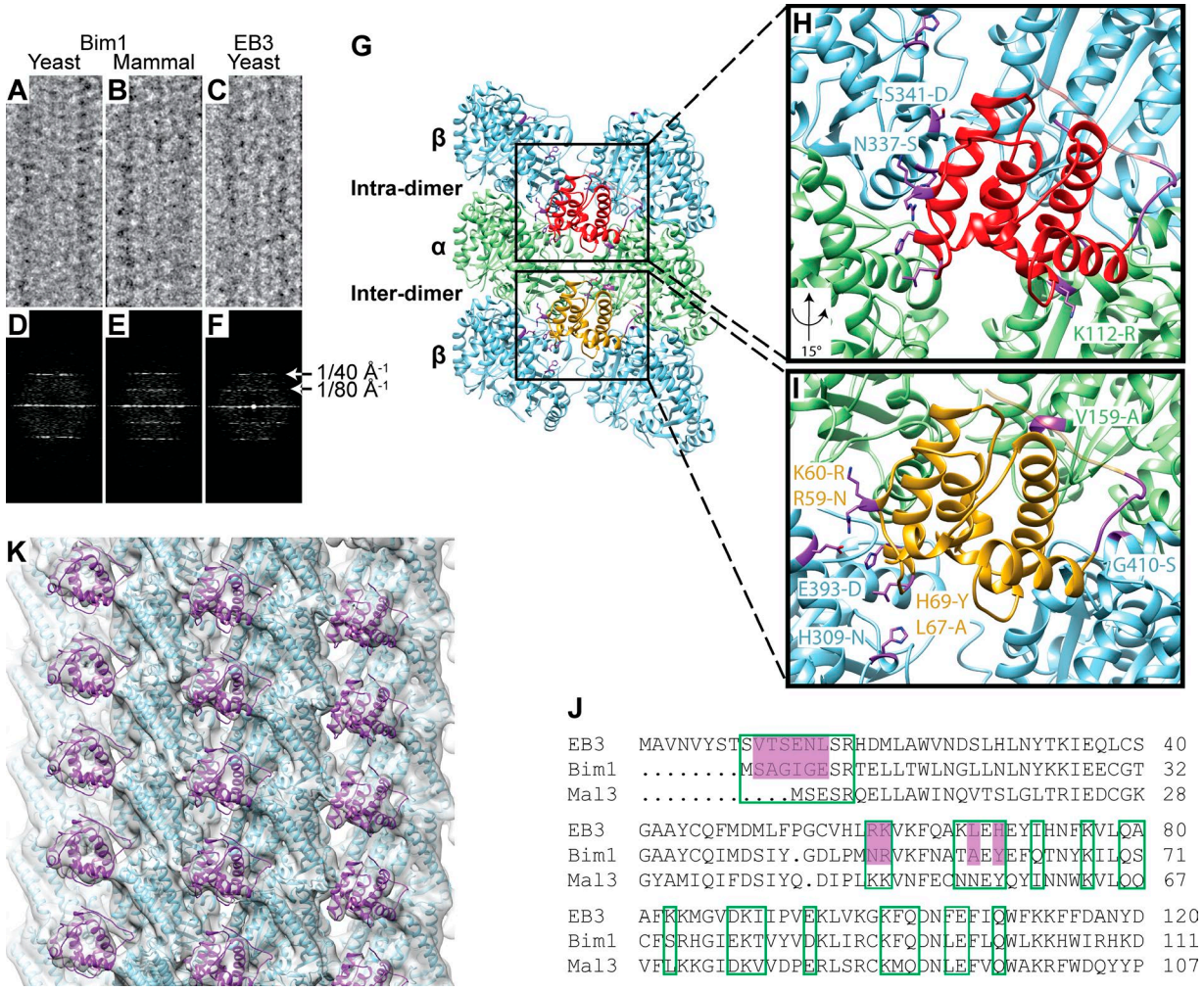

Figure 3. **Bim1 binds yeast microtubules with a monomer repeat binding pattern.** (A–C) Raw images of MTs assembled from yeast (A and C) or mammalian (B) tubulin decorated with the +TIP Bim1 (A and B) or human EB3 (C). (D–F) Corresponding power spectra show the tubulin monomer repeat of 1/40 $Å^{-1}$ but no +TIP repeat at 1/80 $Å^{-1}$ for yeast MTs decorated with Bim1, for which Bim1 binds every tubulin monomer instead of between dimers. (G–I) Schematic (G) showing the extra, noncanonical binding position of +TIP (enlarged in H) at the intradimer contact and the canonical position (enlarged in I) adjacent to the interdimer interface. Analysis of sequence differences between yeast and mammalian proteins shows that both tubulin and +TIP sequence differences likely contribute to this binding pattern. Several significant differences are present on the lefthand side of the CH domain (+TIP residues 67–60). (J) Sequence alignment of +TIP CH domains showing significant amino acid differences involved in contacts (purple) and residues within 4 Å of tubulin (green boxes). The +TIP sequences are less conserved than tubulin, though both contribute to the binding pattern. (K) Reconstruction of yeast GTPγS MT decorated with Bim1 showing Bim1 at both inter- and intradimer sites. Docked EB3 model is shown in purple and tubulin monomers in blue (note that α- and β-tubulin cannot be distinguished in this reconstruction).

al., 2015). The present findings on the special mode of binding of Bim1 on yeast MTs provide structural support for the idea that Bim1 might make species-specific interactions with yeast MTs that are required for robust plus end tracking.

We investigated the structural basis for the binding of the yeast EB protein, Bim1, to GTPγS-bound yeast MTs, using a monomeric construct of Bim1 containing its calponin homology (CH) domain. Initial Fourier analysis of the images showed only layer line signal corresponding to the ∼40-Å tubulin monomer repeat (Fig. 3, A and D), whereas signal corresponding to the ∼80-Å tubulin dimer repeat that is typically seen in the presence of MT-binding partners was absent. This result, which reflects a lack of discrimination of Bim1 for the α- and β-tubulin subunits at the high concentrations used (excess Bim1, 30 µM for 6 µM tubulin), indicates that two Bim1 CH domains bind per αβ-tubulin dimer. Consequently, Bim1 cannot serve as a fiducial for alignment of αβ-tubulin, and therefore α- and β-tubulin are averaged together in the reconstructions of Bim1-bound yeast MTs (Fig. 3 K).

To determine whether binding at the noncanonical, intradimer site was caused by yeast tubulin or the yeast EB protein, we also investigated the binding of Bim1 to mammalian MTs and of mammalian EB3 to yeast MTs (in all cases using GTPγS-bound MTs; Fig. 3, B and E and C and F, respectively). We found that only Bim1 on yeast MTs occupies both interdimer (canonical) and intradimer (noncanonical) sites, which results in the lack of the 1/80 $Å^{-1}$ layer line (Fig. 3 D). In all other cases, the EB protein binds once every tubulin dimer, thus giving rise to signal at 1/80 $Å^{-1}$ in Fourier space. This finding suggests that Bim1 and yeast tubulin have coevolved to accommodate the binding of Bim1 on this noncanonical binding pocket. These changes in sequence and binding mode may also contribute to species specificity in plus end tracking.

Which residues in yeast tubulin or Bim1 could be responsible for this additional interaction? Alignment of the sequences for Bim1 and EB3 (Fig. 3 J) shows changes (R59 to N, K60 to R, L67 to A, and H69 to Y) at positions that mediate interactions between the CH domain of EB3 and MTs (Zhang et al., 2015). These changes in sequence are located on one surface of the CH domain that interacts predominantly with β-tubulin at the canonical interdimer site (Fig. 3 I). Bim1 also has a shorter and very different N-terminal loop preceding the CH domain (Fig. 3 J). Using the atomic model of EB3 bound to the MT (Zhang et al., 2015) as a reference to define the footprint of Bim1 on tubulin, we find no differences in α-tubulin sequence between yeast and mammalian tubulin at the canonical or noncanonical sites of interaction with Bim1. In contrast, two β-tubulin positions involved in EB interactions at the canonical site differ between yeast and mammalian tubulin: H309 to N and E393 to D (Fig. 3 I). Additionally, there are differences in β-tubulin at the noncanonical site that could account for this additional yeast-specific interaction: N337 to S and S341 to D (Fig. 3 H) on one PF and G410 to S on the second PF. These combined changes have the potential to result in an additional binding site of Bim1 to MTs.

To examine the dependence of Bim1 binding on the nucleotide state of tubulin within the MT, we attempted to decorate dynamic yeast MTs (assembled from GTP-bound tubulin) with Bim1. Trapping this state for visualization by cryo-EM turned out to be challenging because of the fast disassembly of MTs when excess Bim1 was present. Although this property seems to be more extreme for the yeast system, it may reflect the faster depolymerization rate of yeast MTs (Geyer et al., 2015) and is generally consistent with previous results of EB proteins increasing the catastrophe frequency of MTs (Maurer et al., 2014). Nevertheless, we managed to capture some MTs before depolymerization occurred, by decreasing the molar ratio of Bim1 to tubulin from 5:1 (used in previous studies) to 2:1 and by vitrifying the sample within 1 min after the addition of Bim1. Our cryo-EM observations allowed us to conclude that Bim1 binds at both the canonical and noncanonical sites, and that the MT lattice becomes compacted in the presence of Bim1 (Table S1).

Conclusions

Our studies have unveiled several differences in the structure and interactions of in vitro–assembled yeast and mammalian MTs. A major observation concerning yeast MT structure is that the lattice observed for the spontaneously nucleated dynamic MTs (assembled in the presence of GTP) was not compacted as seen for mammalian tubulin. The compaction of mammalian MTs is clearly related to GTP hydrolysis, because MTs assembled with GMPCPP do not compact. Although we did not observe a compacted state for dynamic yeast MTs, we did observe compaction for yeast MTs assembled with GTPγS. Similarly, mammalian tubulin assembled with GTPγS also gives rise to a compacted lattice (unpublished data). Thus, it is not the case that the yeast MT lattice is incapable of compaction. Lack of compaction in dynamic yeast MTs might reflect either a difference in GTP hydrolysis or a different conformational response to the GDP state of the lattice. The compaction that we see in yeast MTs assembled from GTPγS tubulin, which we previously proposed to correspond to a GDP-Pi state (Zhang et al., 2015), provides support for the idea that yeast tubulin is able to undergo similar conformational changes in the lattice as mammalian tubulin. Given that the residual GTP content for yeast MTs has been reported to be higher than that of mammalian MTs (Dougherty et al., 1998; Dimitrov et al., 2008; Geyer et al., 2015) in assays where MTs were formed by spontaneous nucleation (without seeds), that we did not observe a fully compacted state of yeast MTs seems to be most simply explained by differences in GTP hydrolysis rates, but we cannot yet rule out alternative mechanisms. One possible scenario entails a combination of effects in which GTP hydrolysis occurs to a lesser extent in yeast, and the coupling of hydrolysis and conformational change is also weaker, or at least distinct in its transmission through the lattice. In fact, these two properties could be intertwined. Although it is clear that for mammalian tubulin, hydrolysis and compaction are linked, unambiguously establishing causality is not simple. Indeed, cooperativity within the lattice may add another level of complexity that is not yet understood for either the mammalian or yeast systems. These are fascinating open questions, answers to which will require data that go beyond the structures of homogeneous states of the MT that have framed our current understanding.

We found that binding of Bim1 to GTPγS yeast MTs slightly compacted the lattice compared with GTPγS without Bim1, indicating that EB proteins can promote compaction independent of changes in nucleotide state/hydrolysis. A prior study of mammalian MTs showed that the Bim1 homolog EB3 caused rapid GMPCPP hydrolysis and lattice compaction (Zhang et al., 2015). In light of this result, we find it interesting that coassembly of Bim1 with dynamic yeast MTs (which we showed to be expanded) resulted in a compact lattice that was also much less stable. Thus, it seems likely that by promoting a more compact form of the GTP lattice, Bim1 increased the rate or extent of GTPase in yeast MTs.

A curious observation is that the yeast Bim1 binds yeast MTs between αβ-tubulin heterodimers, as seen for other organisms, but also within tubulin dimers. Coevolutionary changes in both yeast tubulin and the +TIPs tracking protein Bim1 appear to lead to this unique binding pattern for Bim1. The species-specific binding pattern we observed is consistent with prior results of poor Bim1 tip-tracking on porcine MTs (Molodtsov et al., 2016) but robust tracking of Bim1 on yeast MTs (Geyer et al., 2015). Thus, the differences in sequence and mode of binding across species are likely to be important for the functional interaction of EB proteins with the MT. The species-specific differences in structure and activity we observed are not unique to EB proteins. Of note, species-specific differences in binding stoichiometry have also been observed in cryo-EM studies of Ndc80 kinetochore complexes. Whereas two human Ndc80 complex bind per αβ-tubulin on the MT (Alushin et al., 2010; Wilson-Kubalek et al., 2016), only one *Caenorhabditis elegans* Ndc80 complex binds per tubulin dimer (Wilson-Kubalek et al., 2016). Likewise, species-specific differences in activity have been observed for MT nucleation by γ-tubulin complexes (Kollman et al., 2015) and for MT elongation by the microtubule polymerase Stu2 (Podolski et al., 2014). Given that Bim1 is primarily responsible for recruiting other proteins to the ends of growing MTs, the relevance of its different behavior across species may also extend to +TIP cargoes.

In closing, the high level of sequence conservation between yeast and mammalian tubulin and their conserved structure leads to the prediction that these proteins would have very similar behaviors. However, we find that the cumulative effect of modest residue changes leads to significant differences in the MT lattice. It remains to be seen whether these

in vitro differences result in different MT behavior in vivo for these distant species.

Materials and methods

Reagents

All reagents were purchased from Sigma-Aldrich unless otherwise specified.

Microtubule preparation

Purified porcine tubulin was resuspended and stored as recommended by the manufacturer (T240; Cytoskeleton, Inc.). A yeast strain whose tubulin had been sensitized to Taxol by mutating residues on β-tubulin (strain MGY2) was kindly provided by M. Gupta (Iowa State University, Ames, IA) and was previously described (Gupta et al., 2003). The endogenous tubulin from this strain was purified according to previous protocols (Drummond et al., 2011). Yeast tubulin was purified from inducible overexpressing strains of *S. cerevisiae* using Ni-affinity and ion-exchange chromatography as described previously (Geyer et al., 2015). Tubulin samples were stored in storage buffer (10 mM Pipes, pH 6.9, 1 mM $MgCl_2$, and 1 mM EGTA) containing 50 µM GTP. 6xHis-tagged Bim1-EGFP monomeric construct, comprising Bim1 aa 1–210, was purified according to previous protocols (Zimniak et al., 2009), as was the human EB3 monomer with aa 1–200 (Zhang et al., 2015). The construct for EB1-GFP was generously loaned from the Kapoor laboratory (Rockefeller University, New York, NY). Expression and purification of EB1-GFP was performed as previously described (Forth et al., 2014). Aliquots were stored at −80°C until needed. Aggregates from the freeze-thaw cycle were removed by cold filtration using spin filters (UFC3 0VV 25; Thermo Fisher Scientific) before polymerization. All tubulin was polymerized in BRB80 (80 mM Pipes, pH 6.9, 1 mM EGTA, 1 mM $MgCl_2$, and 1 mM DTT) supplemented with 10% glycerol and 1 mM GTP at 30°C. Taxol (TXD01; Cytoskeleton, Inc.) and epothilone-B (S1364; Selleck Chemicals) were dissolved in DMSO to 2 and 1 mM, respectively. Dynamic microtubules were polymerized for 15 min. To generate GMPCPP and GTPγS MTs, the dynamic MTs were pelleted at 17,000 *g* for 20 min, the supernatant was discarded, and the pellet was resuspended in cold BRB80 buffer with 2 mM of the desired nucleotide and left in ice for 20 min to fully depolymerize and exchange the nucleotide bound to β-tubulin, according to previous protocols (Hyman et al., 1992; Zhang et al., 2015). The sample was then warmed to 30°C for 30 min to polymerize into MTs. Nucleotide exchange was verified by the stability of the resulting MTs. For drug stabilized MTs (Taxol and epothilone), dynamic MTs were first polymerized for 10 min, and approximately twofold molar excess of drug was added and polymerized for another 20 min. To minimize the amount of unpolymerized tubulin in the EM images, all MT samples were pelleted at 17,000 *g* for 20 min before making EM grids, then the pellets were resuspended in BRB80 buffer supplemented with the appropriate nucleotide or drug before vitrification.

Cryo-EM sample preparation and imaging

MTs were applied to a glow-discharged C-flat grid with 1.2-µm holes (Protochips). The Mark IV Vitrobot (FEI) used for sample vitrification was set to 30°C and 100% relative humidity for all samples. Dynamic MTs were resuspended in a 1-mg/ml kinesin monomer solution in warm EM buffer (BRB80 with 1 mM GTP and 0.05% Nonidet-P40) and directly applied to the grid. To decorate dynamic MTs with Bim1, it was necessary to resuspend the pellet in Bim1 and apply to the EM grid and plunge-freeze within 1 min. To prepare grids of stabilized MTs decorated with kinesin monomer, Bim1, or EB3, 2 µl MTs was first applied to the grid, allowed to adhere for 30 s, and then washed twice with 4 µl binding protein to saturate all the binding sites. Final concentrations were 25 µM for kinesin and 30 µM for Bim1 and EB3 proteins. No samples had both kinesin and Bim1/EB3. The grids were then blotted for 4 s with blot force 20 and plunged into ethane slush.

Images were collected on a low-base Titan electron microscope (FEI) operated at 300 kV and equipped with a K2 direct detector (Gatan) using the Leginon automated data-collection pipeline (Suloway et al., 2005). The micrographs have a nominal magnification of 27,500, resulting in a final pixel size of 1.32 Å per pixel. Twenty frames of 300 ms each were collected at a dose rate of 8 e^- per pixel per second, with a total dose of 28 $e^-/Å^2$. The dynamic yeast microtubules decorated with Bim1 that were difficult to capture were imaged on a Tecnai F20 electron microscope (FEI) operated at 120 kV and equipped with a 4k Ultrascan CCD camera (Gatan). Micrographs were collected using Leginon (Suloway et al., 2005) with a dose of 20 $e^-/Å^2$ and nominal magnification of 80,000, giving a final size of 1.37 Å per pixel.

Image analysis and data processing

Images collected from the Titan microscope were processed using the Appion pipeline (Lander et al., 2009), including individual frame alignment using MOTIONCORR (Li et al., 2013), and CTF estimation using CTFFIND4 (Rohou and Grigorieff, 2015). Images from the Tecnai F20 microscope were processed using the same software, except for the individual frame alignment. According to a previously published MT data-processing protocol (Zhang and Nogales, 2015; Zhang et al., 2015), regions of the raw micrographs containing decorated MTs were extracted using overlapping square boxes of 675 Å, spaced 80 Å apart. Each of these boxes was treated as an independent, single particle using iterative helical real space reconstruction (IHRSR; Egelman, 2007). The boxed MT segments were sorted by PF number, and initial 3D alignment parameters were generated using EMAN2 multi-model refinement (Tang et al., 2007) with models of 12, 13, 14, and 15 PF MTs (Sui and Downing, 2010) low-pass filtered to 20-Å resolution, followed by IHRSR to obtain initial 3D reconstructions. Frealign (Lyumkis et al., 2013) was then used to further process the dominant PF number for each MT condition to obtain better alignment parameters. Finally, we applied in-house scripts to determine the seam location (i.e., to align α- and β-tubulin) for particles from the same MT (Zhang and Nogales, 2015). This step was critical in separating α- and β-tubulin.

If our hypothesis, that the lack of compaction for the yeast dynamic MTs is caused by limited hydrolysis within the lattice, is true, then the experimental map for the E-site nucleotide should show additional density to that seen for the GDP state of mammalian MTs. Unfortunately, during our reconstruction of the dynamic MT state, it became apparent that our previously developed methods to identify the α/β-tubulin register and MT seam position were less effective when used on the yeast data; i.e., the final density still showed signs of α/β-tubulin mixing. One possible explanation would be the presence of multiple seams within an MT. Our efforts to investigate such a possibility indicated that this may be the case. After applying the in-house scripts to determine the seam for the 12-PF dynamic MTs (the largest dataset), we then performed maximum likelihood classification without symmetry in Frealign using 24 classes, to account for the possible seam locations and register of αβ-tubulin. Selected classes from this classification are shown in Fig. S3. The uneven kinesin density for certain PFs (Fig. S3 B), even when the dominant seam position is correctly identified and enforced, suggests that some fraction of the MTs might have additional seams. Unfortunately, our current data-processing algorithm cannot handle such cases. Because a certain percentage of α- and β-tubulin are incorrectly averaged together in our yeast MT reconstructions, we could not directly draw the conclusion of lack of hydrolysis based on

the similarity of the densities seen for the E-site and N-site nucleotide. This shortcoming, however, does not exclude the possibility that GTP is only partially hydrolyzed within the yeast MT lattice during assembly.

Note that the possibility of A-lattice MTs was also considered, but no evidence for A-lattices could be found in the power spectra of individual MTs decorated with kinesin or Bim1, as has been previously reported for Mal3-decorated MTs (des Georges et al., 2008).

Local resolution estimates were performed with the Bsoft software package (Heymann and Belnap, 2007) using the whole MT. Half-maps were generated using MT segments separated by MT, rather than even/odd images, to ensure that each half-map did not contain segments from the same MT. Despite similar imaging conditions and amount of data used, the resolution of the drug-stabilized structures (∼4 Å) was clearly worse than that for the dynamic MT reconstruction (3.7 Å; Fig. S2, A and B). Studies of mammalian MTs stabilized with either Taxol or zampanolide, which like epothilone also bind to the Taxol-binding pocket, have recently shown that these two drugs induce lattice flexibility (Kellogg et al., 2017). Together with our present results, these findings suggest that MT-stabilizing agents that bind to the Taxol site induce the same lattice flexibility, whether in yeast or mammalian MTs.

Atomic model refinement

The resolution of our dynamic yeast MT cryo-EM map is sufficient to follow the path of the αβ-tubulin polypeptide chains and place large side chains, but some ambiguity is present for positioning some parts of the main chain and in the assignment of side-chain rotamers. To build the best possible atomic models of yeast tubulin from our cryo-EM density maps, we used Rosetta (DiMaio et al., 2015), which incorporates statistical information from existing structures. The models were then further refined using REFMAC (Brown et al., 2015) and Phenix (Adams et al., 2011) to ensure good geometry. To build an atomic model, the model of an expanded mammalian tubulin heterodimer (Zhang et al., 2015) was first manually fitted into the yeast dynamic MT reconstruction (which had the highest resolution) using Coot (Emsley et al., 2010). Residues were mutated to match the yeast sequence, and regions of poor fit for the main chain were manually adjusted. To capture interactions between neighboring tubulin heterodimers, nine copies of this starting model were fitted into the density to form a 3 × 3 lattice of heterodimers. This results in the central heterodimer having all the appropriate neighbors for forming contacts. The central heterodimer, and the eight identical copies, were then refined using Rosetta (DiMaio et al., 2015). An ensemble of structures (>1,000 structures) was generated to ensure sufficient sampling of possible solutions by Rosetta. The best structure from the ensemble of models was then subjected to minor refinements with Phenix (Adams et al., 2011) and Refmac (Brown et al., 2015) to ensure proper geometry of all amino acids and ligands. The dynamic starting model was used as the initial model for the epothilone and Taxol mutant model. After addition of the appropriate ligand or mutations using Coot, these models were used as initial models to generate Rosetta ensembles. The best models from the ensembles were then refined to generate the final model.

To measure the intra- and interdimer distance for yeast states that did not go through the full model refinement procedure because of the limited resolution of the final map (12-PF GMPCPP and GTPγS and 13-PF dynamic, GMPCPP, and GTPγS), the model for the yeast dynamic tubulin was split into α- and β-monomers with their associated nucleotide, and each monomer was independently fitted as rigid body into the map.

Accession numbers

The following cryo-EM maps and refined atomic models (accession numbers indicated) have been deposited in the Electron Microscopy Data Bank: Dynamic MT (EMDB-8755, PDB entry 5W3F), Taxol MT (EMD-8757, PDB entry 5W3J), Epothilone MT (EMD-8756, PDB entry 5W3H), GTPγS MT (EMD-8759), and GMPCPP (EMD-8758).

Online supplemental material

Fig. S1 shows yeast MT reconstructions. Fig. S2 shows Fourier shell correlation curves, local resolution estimation, and lattice parameters. In Fig. S3, classification of 12-PF data shows uneven PF mixing. Table S1 is a summary of the lattice parameters for each yeast MT state analyzed.

Acknowledgments

We thank Patricia Grob and Tom Houweling for EM and computer support, respectively. Nathaniel Krefman, Itziar Ibarlucea, and Georjana Barnes helped with the purification of the taxol-sensitized yeast tubulin.

B. LaFrance is supported by a National Science Foundation (NSF) Graduate Research Fellowship (1106400). L.M. Rice is the Thomas O. Hicks Scholar in Medical Research. Work in L.M. Rice's laboratory was supported by the NSF (MCB 1054947 and 1615938) and the National Institutes of Health (NIH; R01-GM098543). E.A. Geyer was supported by the NIH (T32 GM008297) and by an NSF Graduate Research Fellowship (2014177758). Work in E. Nogales's laboratory was supported by the NIH (P01-GM051487). E. Nogales is a Howard Hughes Medical Institute Investigator.

The authors declare no competing financial interests.

Author contributions: S.C. Howes provided reagents, collected and analyzed data, and wrote the paper. E.A. Geyer provided reagents and edited the paper. B. LaFrance provided reagents, collected and analyzed data, and edited the paper. R. Zhang analyzed data and edited the paper. E.H. Kellogg analyzed data and edited the paper. S. Westermann provided reagents and edited the paper. L.M. Rice provided reagents and wrote the paper. E. Nogales supervised the work and wrote the paper.

Submitted: 31 December 2016
Revised: 31 March 2017
Accepted: 30 May 2017

References

Adams, P.D., P.V. Afonine, G. Bunkóczi, V.B. Chen, N. Echols, J.J. Headd, L.-W. Hung, S. Jain, G.J. Kapral, R.W. Grosse Kunstleve, et al. 2011. The Phenix software for automated determination of macromolecular structures. *Methods.* 55:94–106. http://dx.doi.org/10.1016/j.ymeth.2011.07.005

Akhmanova, A., and M.O. Steinmetz. 2008. Tracking the ends: A dynamic protein network controls the fate of microtubule tips. *Nat. Rev. Mol. Cell Biol.* 9:309–322. http://dx.doi.org/10.1038/nrm2369

Alushin, G.M., V.H. Ramey, S. Pasqualato, D.A. Ball, N. Grigorieff, A. Musacchio, and E. Nogales. 2010. The Ndc80 kinetochore complex forms oligomeric arrays along microtubules. *Nature.* 467:805–810. http://dx.doi.org/10.1038/nature09423

Alushin, G.M., G.C. Lander, E.H. Kellogg, R. Zhang, D. Baker, and E. Nogales. 2014. High-resolution microtubule structures reveal the structural transitions in αβ-tubulin upon GTP hydrolysis. *Cell.* 157:1117–1129. http://dx.doi.org/10.1016/j.cell.2014.03.053

Ayaz, P., X. Ye, P. Huddleston, C.A. Brautigam, and L.M. Rice. 2012. A TOG:αβ-tubulin complex structure reveals conformation-based mechanisms for a microtubule polymerase. *Science.* 337:857–860. http://dx.doi.org/10.1126/science.1221698

Brown, A., F. Long, R.A. Nicholls, J. Toots, P. Emsley, and G. Murshudov. 2015. Tools for macromolecular model building and refinement into electron cryo-microscopy reconstructions. *Acta Crystallogr. D Biol. Crystallogr.* 71:136–153. http://dx.doi.org/10.1107/S1399004714021683

Conde, C., and A. Cáceres. 2009. Microtubule assembly, organization and dynamics in axons and dendrites. *Nat. Rev. Neurosci.* 10:319–332. http://dx.doi.org/10.1038/nrn2631

Davis, A., C.R. Sage, L. Wilson, and K.W. Farrell. 1993. Purification and biochemical characterization of tubulin from the budding yeast *Saccharomyces cerevisiae*. *Biochemistry.* 32:8823–8835. http://dx.doi.org/10.1021/bi00085a013

Desai, A., and T.J. Mitchison. 1997. Microtubule polymerization dynamics. *Annu. Rev. Cell Dev. Biol.* 13:83–117. http://dx.doi.org/10.1146/annurev.cellbio.13.1.83

des Georges, A., M. Katsuki, D.R. Drummond, M. Osei, R.A. Cross, and L.A. Amos. 2008. Mal3, the *Schizosaccharomyces pombe* homolog of EB1, changes the microtubule lattice. *Nat. Struct. Mol. Biol.* 15:1102–1108. http://dx.doi.org/10.1038/nsmb.1482

DiMaio, F., Y. Song, X. Li, M.J. Brunner, C. Xu, V. Conticello, E. Egelman, T.C. Marlovits, Y. Cheng, and D. Baker. 2015. Atomic-accuracy models from 4.5-Å cryo-electron microscopy data with density-guided iterative local refinement. *Nat. Methods.* 12:361–365. http://dx.doi.org/10.1038/nmeth.3286

Dimitrov, A., M. Quesnoit, S. Moutel, I. Cantaloube, C. Poüs, and F. Perez. 2008. Detection of GTP-tubulin conformation in vivo reveals a role for GTP remnants in microtubule rescues. *Science.* 322:1353–1356. http://dx.doi.org/10.1126/science.1165401

Dougherty, C.A., R.H. Himes, L. Wilson, and K.W. Farrell. 1998. Detection of GTP and Pi in wild-type and mutated yeast microtubules: Implications for the role of the GTP/GDP-Pi cap in microtubule dynamics. *Biochemistry.* 37:10861–10865. http://dx.doi.org/10.1021/bi980677n

Drummond, D.R., S. Kain, A. Newcombe, C. Hoey, M. Katsuki, and R.A. Cross. 2011. Purification of tubulin from the fission yeast *Schizosaccharomyces pombe*. *Methods Mol. Biol.* 777:29–55. http://dx.doi.org/10.1007/978-1-61779-252-6_3

Egelman, E.H. 2007. The iterative helical real space reconstruction method: Surmounting the problems posed by real polymers. *J. Struct. Biol.* 157:83–94. http://dx.doi.org/10.1016/j.jsb.2006.05.015

Emsley, P., B. Lohkamp, W.G. Scott, and K. Cowtan. 2010. Features and development of Coot. *Acta Crystallogr. D Biol. Crystallogr.* 66:486–501. http://dx.doi.org/10.1107/S0907444910007493

Fackenthal, J.D., J.A. Hutchens, F.R. Turner, and E.C. Raff. 1995. Structural analysis of mutations in the *Drosophila* beta 2-tubulin isoform reveals regions in the beta-tubulin molecular required for general and for tissue-specific microtubule functions. *Genetics.* 139:267–286.

Forth, S., K.-C. Hsia, Y. Shimamoto, and T.M. Kapoor. 2014. Asymmetric friction of nonmotor MAPs can lead to their directional motion in active microtubule networks. *Cell.* 157:420–432. http://dx.doi.org/10.1016/j.cell.2014.02.018

Geyer, E.A., A. Burns, B.A. Lalonde, X. Ye, F.-A. Piedra, T.C. Huffaker, and L.M. Rice. 2015. A mutation uncouples the tubulin conformational and GTPase cycles, revealing allosteric control of microtubule dynamics. *eLife.* 4:e10113. http://dx.doi.org/10.7554/eLife.10113

Gupta, M.L. Jr., C.J. Bode, G.I. Georg, and R.H. Himes. 2003. Understanding tubulin-Taxol interactions: Mutations that impart Taxol binding to yeast tubulin. *Proc. Natl. Acad. Sci. USA.* 100:6394–6397. http://dx.doi.org/10.1073/pnas.1131967100

Heald, R., and A. Khodjakov. 2015. Thirty years of search and capture: The complex simplicity of mitotic spindle assembly. *J. Cell Biol.* 211:1103–1111. http://dx.doi.org/10.1083/jcb.201510015

Heymann, J.B., and D.M. Belnap. 2007. Bsoft: Image processing and molecular modeling for electron microscopy. *J. Struct. Biol.* 157:3–18. http://dx.doi.org/10.1016/j.jsb.2006.06.006

Hiller, G., and K. Weber. 1978. Radioimmunoassay for tubulin: A quantitative comparison of the tubulin content of different established tissue culture cells and tissues. *Cell.* 14:795–804. http://dx.doi.org/10.1016/0092-8674(78)90335-5

Hyman, A.A., S. Salser, D.N. Drechsel, N. Unwin, and T.J. Mitchison. 1992. Role of GTP hydrolysis in microtubule dynamics: Information from a slowly hydrolyzable analogue, GMPCPP. *Mol. Biol. Cell.* 3:1155–1167. http://dx.doi.org/10.1091/mbc.3.10.1155

Hyman, A.A., D. Chrétien, I. Arnal, and R.H. Wade. 1995. Structural changes accompanying GTP hydrolysis in microtubules: Information from a slowly hydrolyzable analogue guanylyl-(alpha,beta)-methylene-diphosphonate. *J. Cell Biol.* 128:117–125. http://dx.doi.org/10.1083/jcb.128.1.117

Johnson, V., P. Ayaz, P. Huddleston, and L.M. Rice. 2011. Design, overexpression, and purification of polymerization-blocked yeast αβ-tubulin mutants. *Biochemistry.* 50:8636–8644. http://dx.doi.org/10.1021/bi2005174

Kellogg, E.H., N.M.A. Hejab, S. Howes, P. Northcote, J.H. Miller, J.F. Díaz, K.H. Downing, and E. Nogales. 2017. Insights into the distinct mechanisms of action of taxane and non-taxane microtubule stabilizers from cryo-EM structures. *J. Mol. Biol.* 429:633–646. http://dx.doi.org/10.1016/j.jmb.2017.01.001

Kollman, J.M., C.H. Greenberg, S. Li, M. Moritz, A. Zelter, K.K. Fong, J.-J. Fernandez, A. Sali, J. Kilmartin, T.N. Davis, and D.A. Agard. 2015. Ring closure activates yeast γTuRC for species-specific microtubule nucleation. *Nat. Struct. Mol. Biol.* 22:132–137. http://dx.doi.org/10.1038/nsmb.2953

Kumar, P., and T. Wittmann. 2012. +TIPs: SxIPping along microtubule ends. *Trends Cell Biol.* 22:418–428. http://dx.doi.org/10.1016/j.tcb.2012.05.005

Lander, G.C., S.M. Stagg, N.R. Voss, A. Cheng, D. Fellmann, J. Pulokas, C. Yoshioka, C. Irving, A. Mulder, P.-W. Lau, et al. 2009. Appion: An integrated, database-driven pipeline to facilitate EM image processing. *J. Struct. Biol.* 166:95–102. http://dx.doi.org/10.1016/j.jsb.2009.01.002

Li, X., P. Mooney, S. Zheng, C.R. Booth, M.B. Braunfeld, S. Gubbens, D.A. Agard, and Y. Cheng. 2013. Electron counting and beam-induced motion correction enable near-atomic-resolution single-particle cryo-EM. *Nat. Methods.* 10:584–590. http://dx.doi.org/10.1038/nmeth.2472

Lyumkis, D., A.F. Brilot, D.L. Theobald, and N. Grigorieff. 2013. Likelihood-based classification of cryo-EM images using FREALIGN. *J. Struct. Biol.* 183:377–388. http://dx.doi.org/10.1016/j.jsb.2013.07.005

Machin, N.A., J.M. Lee, and G. Barnes. 1995. Microtubule stability in budding yeast: Characterization and dosage suppression of a benomyl-dependent tubulin mutant. *Mol. Biol. Cell.* 6:1241–1259. http://dx.doi.org/10.1091/mbc.6.9.1241

Maurer, S.P., P. Bieling, J. Cope, A. Hoenger, and T. Surrey. 2011. GTPγS microtubules mimic the growing microtubule end structure recognized by end-binding proteins (EBs). *Proc. Natl. Acad. Sci. USA.* 108:3988–3993. http://dx.doi.org/10.1073/pnas.1014758108

Maurer, S.P., F.J. Fourniol, G. Bohner, C.A. Moores, and T. Surrey. 2012. EBs recognize a nucleotide-dependent structural cap at growing microtubule ends. *Cell.* 149:371–382. http://dx.doi.org/10.1016/j.cell.2012.02.049

Maurer, S.P., N.I. Cade, G. Bohner, N. Gustafsson, E. Boutant, and T. Surrey. 2014. EB1 accelerates two conformational transitions important for microtubule maturation and dynamics. *Curr. Biol.* 24:372–384. http://dx.doi.org/10.1016/j.cub.2013.12.042

Minoura, I., Y. Hachikubo, Y. Yamakita, H. Takazaki, R. Ayukawa, S. Uchimura, and E. Muto. 2013. Overexpression, purification, and functional analysis of recombinant human tubulin dimer. *FEBS Lett.* 587:3450–3455. http://dx.doi.org/10.1016/j.febslet.2013.08.032

Mitchison, T., and M. Kirschner. 1984. Dynamic instability of microtubule growth. *Nature.* 312:237–242. http://dx.doi.org/10.1038/312237a0

Molodtsov, M.I., C. Mieck, J. Dobbelaere, A. Dammermann, S. Westermann, and A. Vaziri. 2016. A force-induced directional switch of a molecular motor enables parallel microtubule bundle formation. *Cell.* 167:539–552.e14. http://dx.doi.org/10.1016/j.cell.2016.09.029

Nogales, E., S.G. Wolf, and K.H. Downing. 1998. Structure of the alpha beta tubulin dimer by electron crystallography. *Nature.* 391:199–203. http://dx.doi.org/10.1038/34465

Podolski, M., M. Mahamdeh, and J. Howard. 2014. Stu2, the budding yeast XMAP215/Dis1 homolog, promotes assembly of yeast microtubules by increasing growth rate and decreasing catastrophe frequency. *J. Biol. Chem.* 289:28087–28093. http://dx.doi.org/10.1074/jbc.M114.584300

Reijo, R.A., E.M. Cooper, G.J. Beagle, and T.C. Huffaker. 1994. Systematic mutational analysis of the yeast beta-tubulin gene. *Mol. Biol. Cell.* 5:29–43. http://dx.doi.org/10.1091/mbc.5.1.29

Richards, K.L., K.R. Anders, E. Nogales, K. Schwartz, K.H. Downing, and D. Botstein. 2000. Structure-function relationships in yeast tubulins. *Mol. Biol. Cell.* 11:1887–1903. http://dx.doi.org/10.1091/mbc.11.5.1887

Rohou, A., and N. Grigorieff. 2015. CTFFIND4: Fast and accurate defocus estimation from electron micrographs. *J. Struct. Biol.* 192:216–221. http://dx.doi.org/10.1016/j.jsb.2015.08.008

Sackett, D.L., K.A. Werbovetz, and N.S. Morrissette. 2010. Isolating tubulin from nonneural sources. *Methods Cell Biol.* 95:17–32. http://dx.doi.org/10.1016/S0091-679X(10)95002-4

Schatz, P.J., F. Solomon, and D. Botstein. 1988. Isolation and characterization of conditional-lethal mutations in the TUB1 alpha-tubulin gene of the yeast *Saccharomyces cerevisiae*. *Genetics.* 120:681–695.

Sui, H., and K.H. Downing. 2010. Structural basis of interprotofilament interaction and lateral deformation of microtubules. *Structure.* 18:1022–1031. http://dx.doi.org/10.1016/j.str.2010.05.010

Suloway, C., J. Pulokas, D. Fellmann, A. Cheng, F. Guerra, J. Quispe, S. Stagg, C.S. Potter, and B. Carragher. 2005. Automated molecular microscopy: The new Leginon system. *J. Struct. Biol.* 151:41–60. http://dx.doi.org/10.1016/j.jsb.2005.03.010

Tang, G., L. Peng, P.R. Baldwin, D.S. Mann, W. Jiang, I. Rees, and S.J. Ludtke. 2007. EMAN2: An extensible image processing suite for electron microscopy. *J. Struct. Biol.* 157:38–46. http://dx.doi.org/10.1016/j.jsb.2006.05.009

Thomas, J.H., N.F. Neff, and D. Botstein. 1985. Isolation and characterization of mutations in the beta-tubulin gene of *Saccharomyces cerevisiae*. *Genetics.* 111:715–734.

Ti, S.-C., M.C. Pamula, S.C. Howes, C. Duellberg, N.I. Cade, R.E. Kleiner, S. Forth, T. Surrey, E. Nogales, and T.M. Kapoor. 2016. Mutations in human tubulin proximal to the kinesin-binding site alter dynamic instability at microtubule plus- and minus-ends. *Dev. Cell.* 37:72–84. http://dx.doi.org/10.1016/j.devcel.2016.03.003

Valenstein, M.L., and A. Roll-Mecak. 2016. Graded control of microtubule severing by tubulin glutamylation. *Cell.* 164:911–921. http://dx.doi.org/10.1016/j.cell.2016.01.019

Ward, J.J., H. Roque, C. Antony, and F. Nédélec. 2014. Mechanical design principles of a mitotic spindle. *eLife.* 3:e03398–e03398.

Widlund, P.O., M. Podolski, S. Reber, J. Alper, M. Storch, A.A. Hyman, J. Howard, and D.N. Drechsel. 2012. One-step purification of assembly-competent tubulin from diverse eukaryotic sources. *Mol. Biol. Cell.* 23:4393–4401. http://dx.doi.org/10.1091/mbc.E12-06-0444

Wilson-Kubalek, E.M., I.M. Cheeseman, and R.A. Milligan. 2016. Structural comparison of the *Caenorhabditis elegans* and human Ndc80 complexes bound to microtubules reveals distinct binding behavior. *Mol. Biol. Cell.* 27:1197–1203. http://dx.doi.org/10.1091/mbc.E15-12-0858

Yoon, Y., and B.R. Oakley. 1995. Purification and characterization of assembly-competent tubulin from *Aspergillus nidulans*. *Biochemistry.* 34:6373–6381. http://dx.doi.org/10.1021/bi00019a016

Zhang, R., and E. Nogales. 2015. A new protocol to accurately determine microtubule lattice seam location. *J. Struct. Biol.* 192:245–254. http://dx.doi.org/10.1016/j.jsb.2015.09.015

Zhang, R., G.M. Alushin, A. Brown, and E. Nogales. 2015. Mechanistic origin of microtubule dynamic instability and its modulation by EB proteins. *Cell.* 162:849–859. http://dx.doi.org/10.1016/j.cell.2015.07.012

Zimniak, T., K. Stengl, K. Mechtler, and S. Westermann. 2009. Phosphoregulation of the budding yeast EB1 homologue Bim1p by Aurora/Ipl1p. *J. Cell Biol.* 186:379–391. http://dx.doi.org/10.1083/jcb.200901036